Article

β-Arsenene Monolayer: A Promising Electrocatalyst for Anodic Chlorine Evolution Reaction

Junxian Liu [1], Jack Jon Hinsch [1], Huajie Yin [2], Porun Liu [1], Huijun Zhao [1] and Yun Wang [1,*]

[1] Centre for Catalysis and Clean Energy, School of Environment and Science, Griffith University, Gold Coast, QLD 4222, Australia; junxian.liu@griffithuni.edu.au (J.L.); jack.hinsch@griffithuni.edu.au (J.J.H.); p.liu@griffith.edu.au (P.L.); h.zhao@griffith.edu.au (H.Z.)

[2] Institute of Solid-State Physics, Chinese Academy of Sciences, Hefei 230031, China; yinhj@issp.ac.cn

[*] Correspondence: yun.wang@griffith.edu.au

Abstract: Materials innovation plays an essential role to address the increasing demands of gaseous chlorine from anodic chlorine evolution reaction (CER) in chlor-alkali electrolysis. In this study, two-dimensional (2D) semiconducting group-VA monolayers were theoretically screened for the electrochemical CER by means of the density functional theory (DFT) method. Our results reveal the monolayered β-arsenene has the ultralow thermodynamic overpotential of 0.068 V for CER, which is close to that of the commercial Ru/Ir-based dimensionally stable anode (DSA) of 0.08 V @ 10 mA cm^{-2} and 0.13 V from experiments and theory, respectively. The change of CER pathways via Cl* intermediate on 2D β-arsenene also efficiently suppresses the parasitical oxygen gas production because of a high theoretical oxygen evolution reaction (OER) overpotential of 1.95 V. Our findings may therefore expand the scope of the electrocatalysts design for CER by using emerging 2D materials.

Keywords: 2D group-VA monolayers; chlorine evolution reaction; electrocatalysis; selectivity

1. Introduction

The chlor-alkali process as the primary means for chlorine (Cl_2) manufacture is one of the largest industrial electrochemical technologies [1,2]. Electrocatalysis is the heart of the cost-intensive chlor-alkali industry since it has the demonstrated capacity for a series of energy-related applications including chlorine evolution reaction (CER), oxygen reduction reaction (ORR), and hydrogen evolution reaction (HER) [3–6]. The anodic CER can be achieved through electrolyzing a concentrated brine solution by applying a direct electric current ($2Cl^- \rightarrow Cl_2 + 2e^-$, U_{CER} = 1.36 V vs. SHE) [3,7]. The development of a high-performance electrocatalyst for CER is essential for its commercialization. Mixed-metal oxides (MMOs) based on noble metals Ru or Ir, such as dimensionally stable anodes (DSAs), have been predominantly used as CER catalysts [8,9]. For example, the TiO_2-sup-ported mixtures of RuO_2 and IrO_2 are the most commonly used electrocatalysts in indus-trial chlorine processes [10,11]. However, the DSA catalysts have a high oxygen evolution reaction (OER) activity [1,12–16]. This is because the OER ($2H_2O \rightarrow O_2 + 2H^+ + 2e^-$, U_{OER} = 1.23 V vs. SHE) is competitive at the anode under typical reaction conditions [9,13,17,18]. In the same potential window of the CER, the concomitant O_2 reduces CER selectivity [19]. As such, the purification of gaseous Cl_2 with the high selectivity of CER becomes a major challenge in chlor-alkali electrolysis. To solve the encountered selectivity issue, one of the most promising strategies is the acidification of electrolyte solutions, as the OER perfor-mance of most electrode materials can be suppressed in an acidic media, while the reversible electrode potential of CER is pH-independent [9,19]. To this end, the screen-ing of novel high-performance CER with high reactivity and selectivity in acidic solution be-comes imperative.

To date, two-dimensional (2D) layered nanostructures have attracted increasing attention using as electrocatalysts, since they expose more active sites and achieve much higher catalytic efficiency [20–27]. Recently, the successful fabrication of few-layer black phosphorus brings group-VA elements (P, As, Sb, and Bi) into the family of 2D materials and inspires research interest on other layered allotropes [28]. For example, Bat-Erdene et al. reported that 2D antimonene nanosheets is an efficient electrocatalyst for the nitrogen reduction reaction (NRR) [29]. Additionally, Ren et al. adopt a favorable liquid exfoliation approach to produce few-layer antimonene and implement a metal-free electrocatalyst for water splitting [30]. Thus, the 2D semiconductor family, composed of group-VA elements, has a great potential for electrocatalysis. Yet, the investigations of this class of materials for the CER are still rare.

In this study, the density functional theory (DFT) was employed to comparatively investigate the CER electrocatalytic performance of 2D group-VA monolayers including phosphorene, arsenene, antimonene, and bismuthene. Here, considering the energetic sta-bility and possible fabrication in experiments, we mainly focus on the α and β phases of group-VA monolayers [31–33]. Our DFT results predict that the 2D β-arsenene monolayer is a promising candidate for CER with the ultralow thermodynamic overpotential of 0.068 V and high selectivity in terms of OER.

2. Results and Discussion

2.1. Cl Adsorption on Group-VA Monolayers

The atomic structures of α and β phases of group-VA monolayers are shown in Figure 1. Their structural parameters are listed in Table 1. Group-VA monolayers with α and β allotropes possess honeycomb structures, where α and β phases are derived from orthorhombic and rhombohedral bulk structures, respectively. The lattice constants and layer thicknesses of all studied group-VA monolayers increase from P to Bi regardless of phase because of the increased atomic radius. For four monolayers with α phase, there are two types of bonds, namely in-plane bond (Bond 1) and out-plane bond (Bond 2), as shown in Figure 1a. It is found that bond lengths of both types gradually increase along the periodic table. For another allotrope β phases, only one type of bond, X−X, can be observed with bond lengths increasing from β-phosphorene (2.26 Å) to β-bismuthene (3.04 Å). All these structural parameters are consistent with reported data in previous studies [31,32].
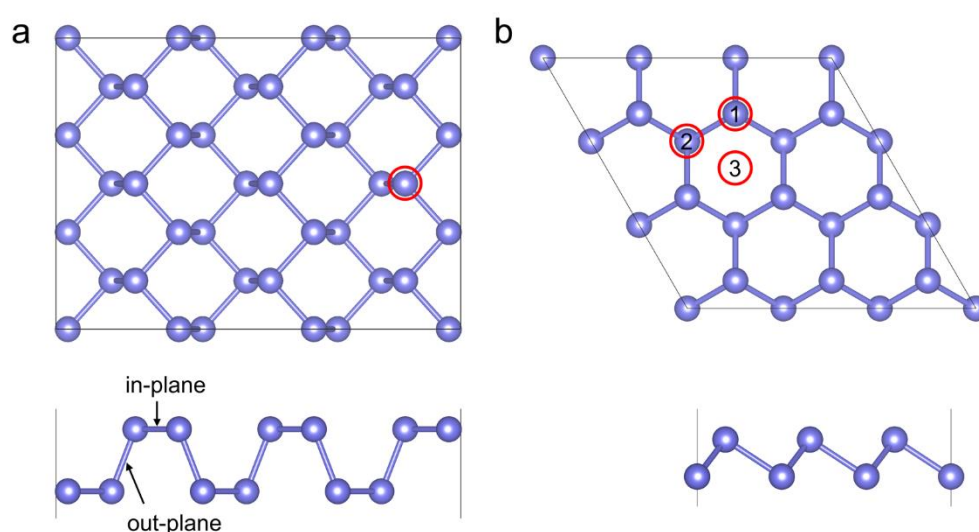
Figure 1. Atomic configurations of all group-VA 2D monolayers. (**a**) α and (**b**) β phase. Red circles represent the different adsorption sites for Cl atoms. Top panel—top view; bottom panel—side view.

Table 1. Structural parameters of all group-VA 2D monolayers. a and b are the lattice constants, d is the thickness of the monolayer, and L denotes the bond lengths.

| Phases		a (Å)	b (Å)	d (Å)	Bonds	L (Å)
P	α	4.59	3.30	2.11	in-plane	2.22
					out-plane	2.26
	β	3.27	3.27	1.24	P−P	2.26
As	α	4.70	3.69	2.41	in-plane	2.51
					out-plane	2.50
	β	3.60	3.60	1.40	As−As	2.51
Sb	α	4.76	4.38	2.83	in-plane	2.94
					out-plane	2.86
	β	4.11	4.11	1.65	Sb−Sb	2.89
Bi	α	4.90	4.58	2.99	in-plane	3.09
					out-plane	3.02
	β	4.33	4.33	1.73	Bi−Bi	3.04

Previous theoretical and experimental studies of the electrocatalytic CER over low-dimensional anodes suggest that the formation of the Cl* intermediate instead of ClO* intermediate would significantly promote the chlorine generation with high selectivity [16–18,34]. Herein, to evaluate the CER performance of group-VA 2D monolayers, the adsorption properties of Cl atoms on both α and β phases were first investigated, and the results are listed in Table 2. As illustrated in Figure 1, one adsorption site (top) of α phase and three different adsorption sites including Site 1 (top), Site 2 (hollow), and Site 3 (hollow) of β phase were considered here to examine the regioselectivity of Cl atoms. It was found that the adsorption on the Site 2 of β-antimonene and Site 3 of β-phosphorene and β-arsenene is unpreferred because the adsorbed Cl atom would migrate to the Site 1 after structural optimization. Moreover, for 2D β-phosphorene and β-arsenene, the Cl adsorptions at Site 1 are much less positive than that of Site 2, indicating that Site 1 is thermodynamically preferred for chlorine adsorption. As a comparison, the Gibbs free energies of Cl* at the Site 3 on β-antimonene and β-bismuthene are much more negative than others, which implies that this hollow site is energetically favored for adsorbing Cl atoms.

Table 2. Calculated average distance between Cl and group-VA atoms (r_{Cl-X}), adsorption energy (ΔE_{Cl*}), and Gibbs free energy change (ΔG_{Cl*}) on different sites of group-VA 2D monolayers with α and β phases.

Structures			r_{Cl-X} (Å)	ΔE_{Cl*} (eV)	ΔG_{Cl*} (eV)
α	P		2.24	−0.315	0.055
	As		2.39	−0.602	−0.232
	Sb		2.55	−1.226	−0.856
	Bi		2.70	−1.336	−0.966
β	P	Site 1	2.21	−0.134	0.236
		Site 2	3.04	0.582	0.952
	As	Site 1	2.37	−0.302	0.068
		Site 2	3.07	0.271	0.641
	Sb	Site 1	2.51	−0.585	−0.215
		Site 3	2.98	−0.602	−0.232
	Bi	Site 1	2.59	−0.797	−0.427
		Site 2	3.20	−0.799	−0.429
		Site 3	3.08	−1.091	−0.721

2.2. CER Activity of Group-VA Monolayers

The electrocatalytic CER is a two-electron process through the Volmer-Heyrovsky mechanism [12,34]. By using the Cl* intermediate, this mechanism can be explained by that Cl* forms first via the adsorption and discharge of a chloride anion in the Volmer step ($* + 2Cl^- \rightarrow Cl^* + Cl^- + e^-$). Thereafter, the Cl* intermediate directly combines with another chloride anion from the electrolyte solution to release gaseous chlorine in the Heyrovsky step ($Cl^* + Cl^- + e^- \rightarrow * + Cl_2 + 2e^-$). Figure 2 depicts the Gibbs free energy changes for CER with the most stable configurations of all monolayers with α and β phases at the equilibrium potential of 1.36 V according to Volmer and Heyrovsky steps. The theoretical overpotential for CER (η_{CER}) can be defined by the ΔG_{Cl^*}, namely $\eta_{CER} = |\Delta G_{Cl^*}|/e$. As shown in Figure 2, the interactions between Cl atoms and α-monolayers are relatively stronger than that of β-monolayers due to the much more negative values of ΔG_{Cl^*}. In the case of α-monolayers, the energy wells of α-arsenene, α-antimonene, and α-bismuthene indicate that the Cl* can form spontaneously. However, the interactions between As, Sb, and Bi and Cl atoms are too strong for efficient Cl_2 desorption. Consequently, the formation of Cl_2 in the Heyrovsky step is energy-demanding for α-arsenene, α-antimonene, and α-bismuthene with the thermodynamic overpotentials of -0.232 V, -0.856 V, and -0.966 V, respectively. As a comparison, the small energy barrier for α-phosphorene implies that the formation of Cl* in the Volmer step is more energy-demanding, leading to a theoretical overpotential of 0.055 V. It demonstrates that the CER mechanisms on α-group VA monolayers can be adjusted by using different elements, and α-phosphorene possesses the highest activity for Cl_2 evolution among these materials.
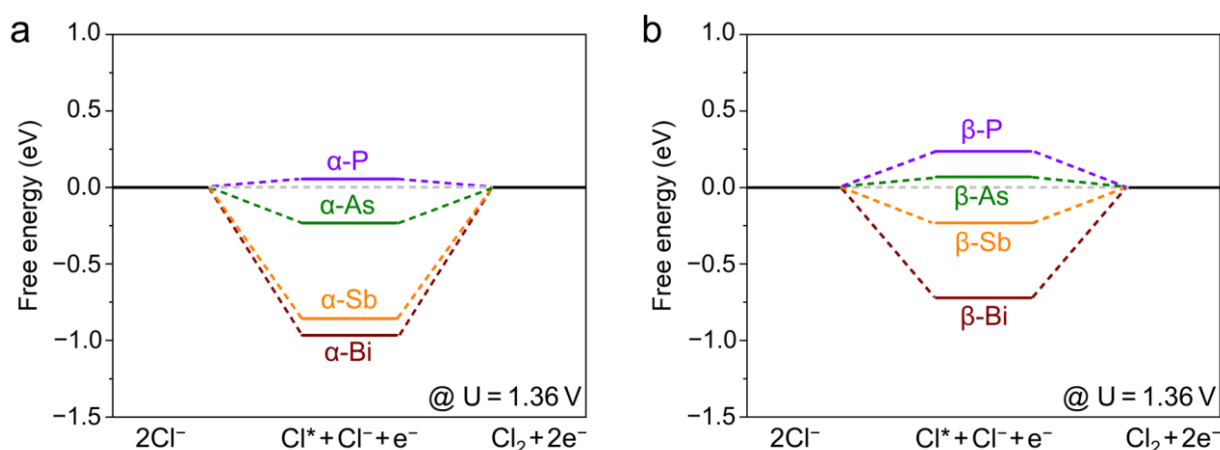
Figure 2. Gibbs free energy diagrams for CER over (**a**) α and (**b**) β phase of group-VA monolayers.

In addition, the CER performances of β-monolayers are quite distinct from α-monolayers due to the totally different atomic structures. Specifically, β-phosphorene has relatively low activity ascribed to its weak binding ability with Cl, whereas β-antimonene and β-bismuthene are anticipated to possess low activity owing to the overly strong adsorption of Cl*. It is notable that β-arsenene has a moderate ΔG_{Cl^*} of 0.068 eV to compromise the reaction barriers in the Cl adsorption and desorption steps, which is beneficial to generate Cl_2 gas. As reported by Exner et al., the CER overpotential of the traditional single-crystalline $RuO_2(110)$ electrocatalyst is 0.13 V vs. SHE via the ClO* precursor [12,14,35]. For better comparison, a summary table including the CER performance for reported electrocatalysts is listed in Table 3. Therefore, our DFT results suggest that the monolayered α-phosphorene and β-arsenene exhibit comparable CER activity compared to that of benchmark $RuO_2(110)$ electrocatalyst.

Table 3. Summary of the experimental (η_{exp}) and thermodynamic overpotentials(η_{td}) of reported electrocatalysts for chlorine evolution [a].

| Electrocatalyst	η_{exp} (mV) @ 10 mA cm^{-2}	η_{td} (V)	Ref.
commercial Ru/Ir-based	105	N/A	[34]
RuO$_2$ (110)	82	0.13	[1,12,14,36]
Ru/Ir/TiO$_2$	>240	N/A	[37]
RuO$_2$@TiO$_2$	~80	N/A	[38]
Ru$_{0.3}$Ti$_{0.7}$O$_2$	~80	N/A	[39]
Co$_3$O$_4$	200	N/A	[40]
CoSb$_2$O$_x$	~300	N/A	[41]
Pt$_1$/CNT	50	0.09	[16,34]
PtO$_2$ (110)	N/A	0.20	[34]
PtNT/CNT	120	N/A	[34]
β-arsenene	N/A	0.068	This work

[a] N/A—not available; CNT—carbon nanotube; NP—nanoparticle.

To deeply understand the CER performances of different group-VA monolayers with α and β phases, the bonding mechanism between the adsorbed Cl and P, As, Sb, or Bi atoms was investigated through the COHP and Mulliken charge analyses. The corresponding COHP images are shown in Figure 3, where covalent bonding and antibonding states are characterized by the positive and negative overlap population, respectively. For obtaining the quantitative description of covalent bonding strength between P, As, Sb, or Bi and Cl atoms, the integral of the −pCOHP (−IpCOHP) up to Fermi energy level was also calculated, shown in Figure 3. The more negative −IpCOHP value suggests that the corresponding active site is more reactive towards the adsorption of Cl via the covalent bonding. However, our results reveal that there is an inverse relationship between the −IpCOHP and ΔG_{Cl*}, suggesting that the covalent bonding strength is not a reasonable descriptor for CER activity of α and β phases of group-VA monolayers. Therefore, we fur-ther investigate their ionic bonding strength, which can be described by the electrostatic attractions (F_{es}) between the P, As, Sb, or Bi and Cl atoms, as well as their bond length, as follows:

$$F_{es} = K\frac{\left|q_X \times q_{Cl}\right|}{r^2_{Cl\text{-}X}} \tag{1}$$

where K is Coulomb's constant, and q_X and q_{Cl} are the Mulliken charges of group VA element X (X = P, As, Sb, or Bi) and Cl, respectively, and the $r_{Cl\text{-}X}$ is the bond length between Cl and X atoms. As listed in Table 4, the trend of −IpCOHP values follows the rule of P < As < Sb < Bi for all α- and β-monolayers, agreeing with the corresponding binding affinity of Cl atom. It demonstrates that the electrostatic attraction between group VA elements and Cl can be a reliable descriptor to predict the CER performance of all studied α- and β-monolayers, which is in agreement with our previous study [42].

To clearly visualize the X−Cl interaction, the electron localization function (ELF) of α- and β-monolayers with the Cl* was calculated, as displayed in Figure 4. The color denotes the renormalized ELF values, with the values 1.0 and 0.5 representing fully localized and fully delocalized electrons, respectively, while the value 0 means very low charge density. Since the electrons are gradually highly delocalized, it is found that the ionic bonding characters between X and Cl atoms increase with the increase of the atomic number. This can be ascribed to the gradually enhanced metallicity from P to Bi atoms, resulting from their decreased electronegativity. The atom with relatively strong metallicity would give rise to much stronger X−Cl interaction, such as Sb and Bi, which is detrimental to the desorption of Cl$_2$ gas. In contrast, the monolayers comprised of the non-metallic atom, such as α-phosphorene and β-arsenene, have the weaker X−Cl interaction to benefit the Cl desorption, resulting in the relatively high activity of Cl$_2$ generation.
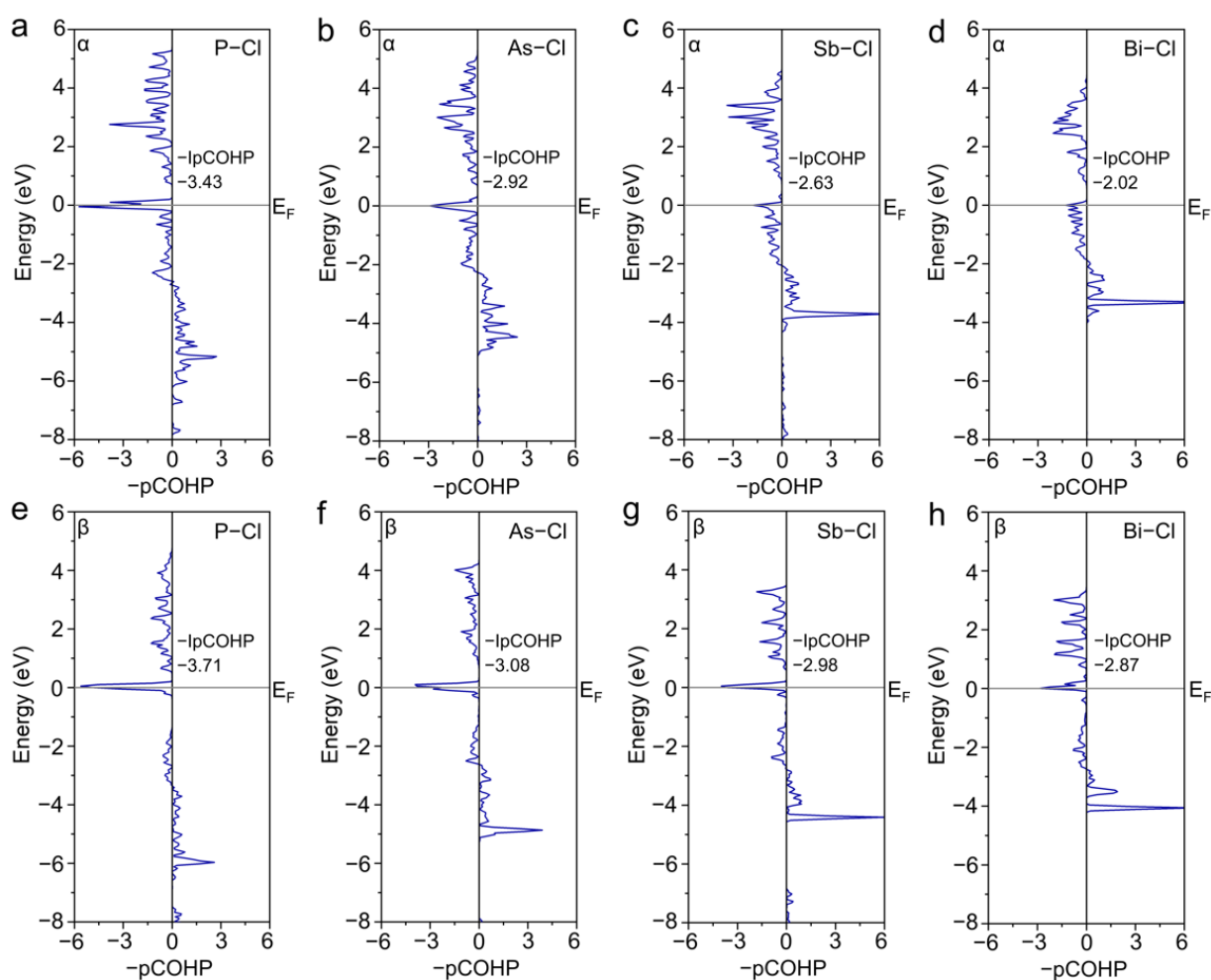
**Figure 3.** COHP analyses of the chemical bonding between the adsorbed chlorine and group-VA element for (**a**) α-phosphorene; (**b**) α-arsenene; (**c**) α-antimonene; (**d**) α-bismuthene; (**e**) β-phosphorene; (**f**) β-arsenene; (**g**) β-antimonene; and (**h**) β-bismuthene monolayers, with the adsorbed Cl atom. The bonding and antibonding states are positive and negative of −pCOHP, respectively. The corresponding integral of −pCOHP (−IpCOHP) values are also provided.

Table 4. The bond lengths of Cl and group-VA atoms (r_{Cl-X}), Mulliken charges of the adsorbed Cl atom (q_{Cl}) and group-VA atoms (q_X), and electrostatic attractions (F_{es}) of all α- and β-monolayers with the adsorbed Cl.

Structures		r_{Cl-X} (Å)	q_{Cl} (e)	q_X (e)	F_{es} (eV/Å)
A	P	2.24	−0.35	0.19	0.19
	As	2.39	−0.43	0.20	0.22
	Sb	2.55	−0.51	0.26	0.29
	Bi	2.70	−0.56	0.29	0.32
B	P	2.21	−0.29	0.25	0.21
	As	2.37	−0.37	0.25	0.24
	Sb	2.51	−0.44	0.35	0.35
	Bi	2.59	−0.48	0.38	0.39
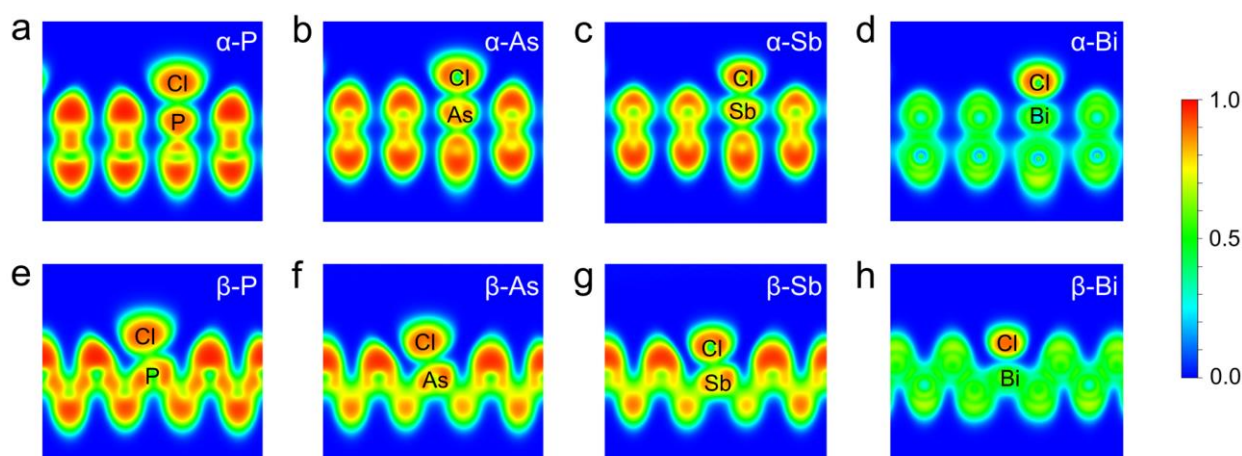
Figure 4. The electron localization functions for (**a**) α-phosphorene; (**b**) α-arsenene; (**c**) α-antimonene; (**d**) α-bismuthene; (**e**) β-phosphorene; (**f**) β-arsenene; (**g**) β-antimonene; and (**h**) β-bismuthene monolayers with the adsorbed Cl atom.

2.3. CER Selectivity

The evolution of gaseous oxygen at the anode is more thermodynamically preferred on account of the relatively lower potential U_{OER} of 1.23 V vs. SHE, which regrettably causes the selectivity problem of Cl_2 gas production at the anode. Therefore, it should combine the high activity with selectivity in an acidic electrolyte for a desired CER electrocatalyst. Since the α-phosphorene and β-arsenene are predicted to have the best performance towards Cl_2 generation, the selectivity of these two monolayers for CER is further analyzed. According to the CHE method, the OER proceeds in the four-electron transfer steps, as follows:

$$* + H_2O \rightarrow HO* + H^+ + e^- \tag{2}$$

$$HO* \rightarrow O* + H^+ + e^- \tag{3}$$

$$O* + H_2O \rightarrow HOO* + H^+ + e^- \tag{4}$$

$$HOO* \rightarrow * + O_2 + H^+ + e^- \tag{5}$$
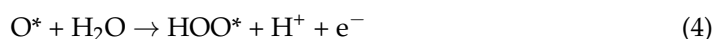
During the OER process, intermediates of HO*, O*, and HOO* are formed in turn following corresponding elementary steps. In this study, we used the adsorption free energy of HO* intermediate forming in the first elementary step of OER to evaluate the se-lectivity for α-phosphorene and β-arsenene monolayers. Figure 5a shows the Gibbs free energy changes of HO* and Cl* species of α-phosphorene and β-arsenene as a function of applied potential U_{SHE} to determine the more energetically stable structures at pH = 0. It is observed that the value of ΔG_{HO*} of α-phosphorene monolayer is smaller than that of ΔG_{Cl*}, implying that the formation of HO* intermediate on the α-phosphorene is more energetically favorable in acidic solution. This indicates that the OER process is preferred on the α-phosphorene monolayer at the potential region of U_{CER}, leading to a poor selectivity of Cl_2. As a comparison, the value of ΔG_{Cl*} of β-arsenene monolayer is much lower than that of ΔG_{HO*}, suggesting that the CER process priors to the OER with the more thermodynamically favorable Cl* precursor.
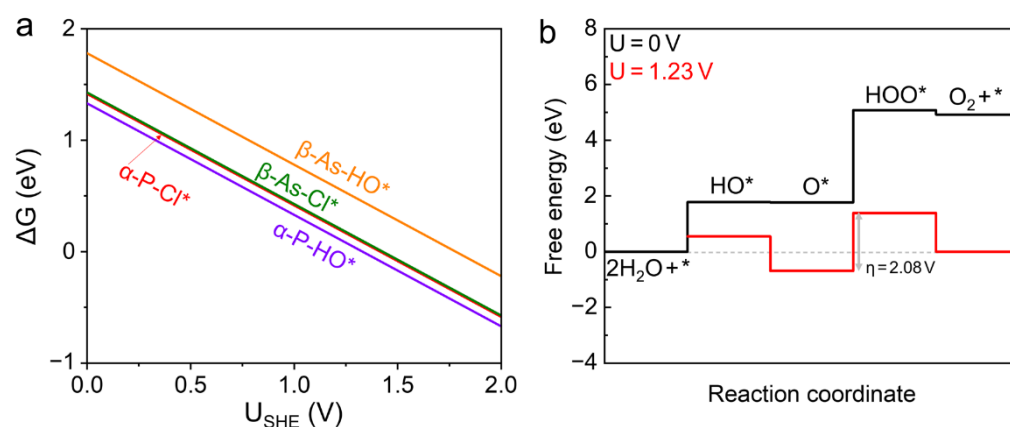
Figure 5. (**a**) The adsorption free energy for Cl* and HO* on α-phosphorene and β-arsenene monolayers as a function of the theoretical standard hydrogen electrode potential (U_{SHE}) at pH = 0; (**b**) Gibbs free energy diagram for OER on β-arsenene monolayer.

To better understand the selectivity of β-arsenene 2D monolayer towards CER, the free energy diagram of the detrimental OER was also calculated, as shown in Figure 5b. The theoretical overpotential of OER is derived from the most energy-demanding step of four elementary reactions Equations (2)–(5). The reaction free energy of Equations (2)–(5) for OER can be defined as follows:

$$\Delta G_1 = \Delta G_{HO^*} \tag{6}$$

$$\Delta G_2 = \Delta G_{O^*} - \Delta G_{HO^*} \tag{7}$$

$$\Delta G_3 = \Delta G_{HOO^*} - \Delta G_{O^*} \tag{8}$$

$$\Delta G_4 = 4.92 - \Delta G_{HOO^*} \tag{9}$$

Therefore, the η_{OER} can be calculated by

$$\eta_{OER} = \frac{\max\left[\Delta G_1, \Delta G_2, \Delta G_3, \Delta G_4\right]}{e} - 1.23 \tag{10}$$

The formation of HOO* intermediate from O* is found to be the most endothermic step, resulting in the potential determining step (PDS) with an extremely large theoretical overpotential of 2.08 V at U_{OER} = 1.23 V. To be referenced to the same potential of CER (U_{CER} = 1.36 V), the corrected theoretical overpotential of OER for β-arsenene monolayer is 1.95 V, i.e., η_{OER} = 2.08 − (1.36 − 1.23) = 1.95 V. It reveals that the OER is efficiently suppressed on the 2D β-arsenene monolayer even in the absence of Cl⁻. In comparison, previous studies demonstrate that the widely used CER electrocatalyst $RuO_2(110)$ is also highly active for oxygen evolution [43,44]. Our DFT results show that the thermodynamic OER overpotential of β-arsenene monolayer is five times larger than that of $RuO_2(110)$ [12], indicating that the selectivity problem can be solved by using β-arsenene monolayer as the CER electrocatalysts. Such an improved selectivity of Cl_2 generation can be ascribed to the inherently different pathways for CER. Unlike $RuO_2(110)$, by virtue of the ClO* intermediate, the CER on β-arsenene monolayer is via Cl* species, which is beneficial to the selective chlorine evolution.

3. Computational Methods

All first principles DFT calculations were performed using the Vienna Ab initio Simulation Package (VASP) based on the projector-augmented wave (PAW) method [45,46]. The exchange-correlation energy was treated by the Perdew-Burke-Ernzerhof (PBE) functional at the generalized gradient approximation (GGA) level [47]. The electron-ion interaction was described using the PAW potentials [48], $3s^2 3p^3$ for P, $4s^2 4p^3$ for As, $5s^2 5p^3$ for Sb,

$6s^2 5d^{10} 6p^3$ for Bi, $3s^2 3p^5$ for Cl, $2s^2 2p^4$ for O, and $1s^1$ for H, respectively. In order to incorporate the effects of nonlocal van der Waals interactions that are not included correctly in conventional DFT calculations, the DFT-D3 method was adopted for dispersion corrections here [49–53]. A plane-wave basis set with the cut-off kinetic energy of 520 eV is employed to expand the smooth part of wave functions. The gamma-centered k-point meshes with a reciprocal space resolution of $2\pi \times 0.03$ Å^{-1} and $2\pi \times 0.02$ Å^{-1} were utilized for structural optimization and static self-consistent calculations, respectively. To model the α and β phases of group-VA monolayers in this study, a (3×3) supercell was adopted, including 36 and 18 group-VA element atoms for α and β phases monolayers, respectively. A 20 Å vacuum along z-direction was applied to prevent spurious interaction between the periodically repeated images. All atoms were allowed to relax until the Hellmann−Feynman forces were smaller than 0.01 eV/Å, and the convergence criterion for the electronic self-consistent loop was set to 10^{-5} eV. The projected crystal orbital Hamilton population (pCOHP) method was used via the LOBSTER program to understand the chemical bonding between group-VA elements (P, As, Sb or Bi) and adsorbed Cl atoms [54–58].

The adsorption energy (ΔE) of all considered adsorbates (i.e., Cl*, HO*, O*, and HOO*, * refers to the corresponding catalytic site) can be calculated by following equations:

$$* + H_2O \rightarrow O* + 2(H^+ + e^-) \tag{11}$$

$$* + H_2O \rightarrow HO* + H^+ + e^- \tag{12}$$

$$* + 2H_2O \rightarrow HOO* + 3(H^+ + e^-) \tag{13}$$

$$* + Cl^- \rightarrow Cl* + e^- \tag{14}$$
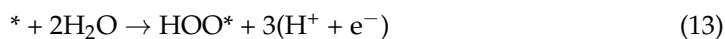
Hence, ΔE for each species was calculated as follows:

$$\Delta E_{O*} = E_{O*} + E_{H_2} - E* - E_{H_2O} \tag{15}$$

$$\Delta E_{HO*} = E_{HO*} + 0.5E_{H_2} - E* - E_{H_2O} \tag{16}$$

$$\Delta E_{HOO*} = E_{HOO*} + 1.5E_{H_2} - E* - 2E_{H_2O} \tag{17}$$

$$\Delta E_{Cl*} = E_{Cl*} - E* - 0.5E_{Cl_2} \tag{18}$$

The free energy change (ΔG) of the considered adsorbates (i.e., Cl*, HO*, O*, and HOO*) was obtained by using the computational hydrogen electrode (CHE) method [59], which can be explained as follows:

$$\Delta G = \Delta E + \Delta ZPE - T\Delta S \tag{19}$$

where ΔZPE is the change in zero-pint vibrational energy and −TΔS is the entropy contribution at room temperature. In this study, we considered the standard conditions of a_{Cl^-} = 1 and pH = 0. Therefore, the ΔG for each species as a function of applied potential U_{SHE} can be defined as follows at 298 K:

$$\Delta G\,(U) = \Delta E + \Delta ZPE - T\Delta S - \nu(e^-) \cdot e \cdot U_{SHE} - \nu(Cl^-) \cdot e \cdot U_{Cl} \tag{20}$$

where $\nu(e^-)$, and $\nu(Cl^-)$ are the values for stoichiometric coefficient of transferred electrons and chloride of corresponding adsorption intermediates, respectively; U_{Cl} is the standard potential of the reversible chlorine electrode (1.36 V at 298 K); and U_{SHE} denotes the applied electrode potential referenced to standard hydrogen electrode (SHE).

4. Conclusions

In summary, the first-principle DFT calculations were performed to investigate the CER performance of 2D α and β phases of group-VA monolayers. Our calculated results reveal that β-arsenene monolayer exhibits high activity and selectivity of gaseous Cl_2 generation by virtue of the expected Cl* precursor, with the thermodynamic overpotential

of 0.068 V and 1.95 V for the CER and OER, respectively. This 2D β-arsenene monolayered catalyst may therefore be a promising candidate for CER in the acidic medium. Moreover, our results found that the COHP analyses fail to predict the CER performance of these α and β phases of group-VA monolayers, since the covalent bonding state between adsorbent and Cl atoms becomes weaker from P to Bi. The electrostatic attraction between adsorbent and Cl atoms is a better descriptor for these systems. The theoretical prediction of this study may broaden the scope of CER electrocatalysts design using 2D materials.

Author Contributions: Methodology, software, formal analysis, writing—original draft preparation, J.L.; writing—review and editing, J.J.H.; writing—review and editing, H.Y.; writing—review and editing, P.L.; project administration, writing—review and editing, H.Z.; project administration, supervision, conceptualization, methodology, resources, writing—review and editing, Y.W. All authors have read and agreed to the published version of the manuscript.

Conflicts of Interest: The authors declare no conflict of interest.

References

1. Sohrabnejad-Eskan, I.; Goryachev, A.; Exner, K.S.; Kibler, L.A.; Hensen, E.J.M.; Hofmann, J.P.; Over, H. Temperature-Dependent Kinetic Studies of the Chlorine Evolution Reaction over RuO_2(110) Model Electrodes. *ACS Catal.* **2017**, *7*, 2403–2411. [CrossRef]
2. Karlsson, R.K.; Cornell, A. Selectivity between Oxygen and Chlorine Evolution in the Chlor-Alkali and Chlorate Processes. *Chem. Rev.* **2016**, *116*, 2982–3028. [CrossRef] [PubMed]
3. Wang, Y.; Liu, Y.; Wiley, D.; Zhao, S.; Tang, Z. Recent advances in electrocatalytic chloride oxidation for chlorine gas production. *J. Mater. Chem. A* **2021**, *9*, 18974–18993. [CrossRef]
4. Bhalothia, D.; Lin, C.-Y.; Yan, C.; Yang, Y.-T.; Chen, T.-Y. Effects of Pt metal loading on the atomic restructure and oxygen reduction reaction performance of Pt-cluster decorated Cu@Pd electrocatalysts. *Sustain. Energy Fuels* **2019**, *3*, 1668–1681. [CrossRef]
5. Bhalothia, D.; Krishnia, L.; Yang, S.-S.; Yan, C.; Hsiung, W.-H.; Wang, K.-W.; Chen, T.-Y. Recent Advancements and Future Prospects of Noble Metal-Based Heterogeneous Nanocatalysts for Oxygen Reduction and Hydrogen Evolution Reactions. *Appl. Sci.* **2020**, *10*, 7708. [CrossRef]
6. Bhalothia, D.; Huang, T.-H.; Chang, C.-W.; Lin, T.-H.; Wu, S.-C.; Wang, K.-W.; Chen, T.-Y. High-Performance and Stable Hydrogen Evolution Reaction Achieved by Pt Trimer Decoration on Ultralow-Metal Loading Bimetallic PtPd Nanocatalysts. *ACS Appl. Energy Mater.* **2020**, *3*, 11142–11152. [CrossRef]
7. Novak, D.; Tilak, B.; Conway, B. Fundamental and applied aspects of anodic chlorine production. *Mod. Asp. Electrochem.* **1982**, 195–318.
8. Trasatti, S. Electrocatalysis: Understanding the success of DSA®. *Electrochim. Acta* **2000**, *45*, 2377–2385. [CrossRef]
9. Vos, J.G.; Wezendonk, T.A.; Jeremiasse, A.W.; Koper, M.T.M. MnO_x/IrO_x as Selective Oxygen Evolution Electrocatalyst in Acidic Chloride Solution. *J. Am. Chem. Soc.* **2018**, *140*, 10270–10281. [CrossRef]
10. Vos, J.G.; Koper, M.T.M. Measurement of competition between oxygen evolution and chlorine evolution using rotating ring-disk electrode voltammetry. *J. Electroanal. Chem.* **2018**, *819*, 260–268. [CrossRef]
11. Exner, K.S.; Anton, J.; Jacob, T.; Over, H. Microscopic Insights into the Chlorine Evolution Reaction on RuO_2(110): A Mechanistic Ab Initio Atomistic Thermodynamics Study. *Electrocatalysis* **2015**, *6*, 163–172. [CrossRef]
12. Exner, K.S.; Anton, J.; Jacob, T.; Over, H. Controlling selectivity in the chlorine evolution reaction over RuO_2-based catalysts. *Angew. Chem. Int. Ed.* **2014**, *53*, 11032–11035. [CrossRef] [PubMed]
13. Vos, J.G.; Liu, Z.; Speck, F.D.; Perini, N.; Fu, W.; Cherevko, S.; Koper, M.T.M. Selectivity Trends Between Oxygen Evolution and Chlorine Evolution on Iridium-Based Double Perovskites in Acidic Media. *ACS Catal.* **2019**, *9*, 8561–8574. [CrossRef]
14. Exner, K.S. Controlling Stability and Selectivity in the Competing Chlorine and Oxygen Evolution Reaction over Transition Metal Oxide Electrodes. *ChemElectroChem* **2019**, *6*, 3401–3409. [CrossRef]
15. Exner, K.S.; Anton, J.; Jacob, T.; Over, H. Full Kinetics from First Principles of the Chlorine Evolution Reaction over a RuO_2 (110) Model Electrode. *Angew. Chem. Int. Ed.* **2016**, *55*, 7501–7504. [CrossRef]
16. Lim, T.; Kim, J.H.; Kim, J.; Baek, D.S.; Shin, T.J.; Jeong, H.Y.; Lee, K.-S.; Exner, K.S.; Joo, S.H. General Efficacy of Atomically Dispersed Pt Catalysts for the Chlorine Evolution Reaction: Potential-Dependent Switching of the Kinetics and Mechanism. *ACS Catal.* **2021**, *11*, 12232–12246. [CrossRef]
17. Exner, K.S. Beyond Dimensionally Stable Anodes: Single-Atom Catalysts with Superior Chlorine Selectivity. *ChemElectroChem* **2020**, *7*, 1528–1530. [CrossRef]

18. Exner, K.S. Design criteria for the competing chlorine and oxygen evolution reactions: Avoid the OCl adsorbate to enhance chlorine selectivity. *Phys. Chem. Chem. Phys.* **2020**, *22*, 22451–22458. [CrossRef]

19. Exner, K.S. Beyond the Traditional Volcano Concept: Overpotential-Dependent Volcano Plots Exemplified by the Chlorine Evolution Reaction over Transition-Metal Oxides. *J. Phys. Chem. C* **2019**, *123*, 16921–16928. [CrossRef]

20. Gupta, U.; Rao, C.N.R. Hydrogen generation by water splitting using MoS2 and other transition metal dichalcogenides. *Nano Energy* **2017**, *41*, 49–65. [CrossRef]

21. Faber, M.S.; Jin, S. Earth-abundant inorganic electrocatalysts and their nanostructures for energy conversion applications. *Energy Environ. Sci.* **2014**, *7*, 3519–3542. [CrossRef]

22. Qiu, W.; Xie, X.Y.; Qiu, J.; Fang, W.H.; Liang, R.; Ren, X.; Ji, X.; Cui, G.; Asiri, A.M.; Cui, G.; et al. High-performance artificial nitrogen fixation at ambient conditions using a metal-free electrocatalyst. *Nat. Commun.* **2018**, *9*, 3485. [CrossRef] [PubMed]

23. Zhang, L.; Ji, X.; Ren, X.; Ma, Y.; Shi, X.; Tian, Z.; Asiri, A.M.; Chen, L.; Tang, B.; Sun, X. Electrochemical Ammonia Synthesis via Nitrogen Reduction Reaction on a MoS2 Catalyst: Theoretical and Experimental Studies. *Adv. Mater.* **2018**, *30*, e1800191. [CrossRef] [PubMed]

24. Zhang, F.; Zhu, Y.; Tang, C.; Chen, Y.; Qian, B.; Hu, Z.; Chang, Y.C.; Pao, C.W.; Lin, Q.; Kazemi, S.A.; et al. High-Efficiency Electrosynthesis of Hydrogen Peroxide from Oxygen Reduction Enabled by a Tungsten Single Atom Catalyst with Unique Terdentate N_1O_2 Coordination. *Adv. Funct. Mater.* **2021**, 2110224. [CrossRef]

25. Khan, K.; Yan, X.; Yu, Q.; Bae, S.-H.; White, J.J.; Liu, J.; Liu, T.; Sun, C.; Kim, J.; Cheng, H.-M.; et al. Stone-Wales defect-rich carbon-supported dual-metal single atom sites for Zn-air batteries. *Nano Energy* **2021**, *90*, 106488. [CrossRef]

26. Ramalingam, V.; Varadhan, P.; Fu, H.C.; Kim, H.; Zhang, D.; Chen, S.; Song, L.; Ma, D.; Wang, Y.; Alshareef, H.N.; et al. Heteroatom-Mediated Interactions between Ruthenium Single Atoms and an MXene Support for Efficient Hydrogen Evolution. *Adv. Mater.* **2019**, *31*, e1903841. [CrossRef]

27. Xiong, Q.; Wang, Y.; Liu, P.F.; Zheng, L.R.; Wang, G.; Yang, H.G.; Wong, P.K.; Zhang, H.; Zhao, H. Cobalt Covalent Doping in MoS_2 to Induce Bifunctionality of Overall Water Splitting. *Adv. Mater.* **2018**, *30*, e1801450. [CrossRef]

28. Li, L.; Yu, Y.; Ye, G.J.; Ge, Q.; Ou, X.; Wu, H.; Feng, D.; Chen, X.H.; Zhang, Y. Black phosphorus field-effect transistors. *Nat Nanotechnol* **2014**, *9*, 372–377. [CrossRef] [PubMed]

29. Bat-Erdene, M.; Xu, G.; Batmunkh, M.; Bati, A.S.R.; White, J.J.; Nine, M.J.; Losic, D.; Chen, Y.; Wang, Y.; Ma, T.; et al. Surface oxidized two-dimensional antimonene nanosheets for electrochemical ammonia synthesis under ambient conditions. *J. Mater. Chem. A* **2020**, *8*, 4735–4739. [CrossRef]

30. Ren, X.; Li, Z.; Qiao, H.; Liang, W.; Liu, H.; Zhang, F.; Qi, X.; Liu, Y.; Huang, Z.; Zhang, D.; et al. Few-Layer Antimonene Nanosheet: A Metal-Free Bifunctional Electrocatalyst for Effective Water Splitting. *ACS Appl. Energy Mater.* **2019**, *2*, 4774–4781. [CrossRef]

31. Zhang, S.; Xie, M.; Li, F.; Yan, Z.; Li, Y.; Kan, E.; Liu, W.; Chen, Z.; Zeng, H. Semiconducting Group 15 Monolayers: A Broad Range of Band Gaps and High Carrier Mobilities. *Angew. Chem. Int. Ed.* **2016**, *55*, 1666–1669. [CrossRef] [PubMed]

32. Pumera, M.; Sofer, Z. 2D Monoelemental Arsenene, Antimonene, and Bismuthene: Beyond Black Phosphorus. *Adv. Mater.* **2017**, *29*, 1605299. [CrossRef] [PubMed]

33. Xu, J.H.; Wang, E.G.; Ting, C.S.; Su, W.P. Tight-binding theory of the electronic structures for rhombohedral semimetals. *Phys. Rev. B* **1993**, *48*, 17271–17279. [CrossRef] [PubMed]

34. Lim, T.; Jung, G.Y.; Kim, J.H.; Park, S.O.; Park, J.; Kim, Y.T.; Kang, S.J.; Jeong, H.Y.; Kwak, S.K.; Joo, S.H. Atomically dispersed Pt-N_4 sites as efficient and selective electrocatalysts for the chlorine evolution reaction. *Nat. Commun.* **2020**, *11*, 412. [CrossRef]

35. Exner, K.S.; Sohrabnejad-Eskan, I.; Over, H. A Universal Approach To Determine the Free Energy Diagram of an Electrocatalytic Reaction. *ACS Catal.* **2018**, *8*, 1864–1879. [CrossRef]

36. Exner, K.S.; Anton, J.; Jacob, T.; Over, H. Chlorine Evolution Reaction on RuO2(110): Ab initio Atomistic Thermodynamics Study-Pourbaix Diagrams. *Electrochim. Acta* **2014**, *120*, 460–466. [CrossRef]

37. Menzel, N.; Ortel, E.; Mette, K.; Kraehnert, R.; Strasser, P. Dimensionally Stable Ru/Ir/TiO2-Anodes with Tailored Mesoporosity for Efficient Electrochemical Chlorine Evolution. *ACS Catal.* **2013**, *3*, 1324–1333. [CrossRef]

38. Jiang, M.; Wang, H.; Li, Y.; Zhang, H.; Zhang, G.; Lu, Z.; Sun, X.; Jiang, L. Superaerophobic RuO2 -Based Nanostructured Electrode for High-Performance Chlorine Evolution Reaction. *Small* **2017**, *13*, 1602240. [CrossRef]

39. Chen, R.; Trieu, V.; Natter, H.; Stöwe, K.; Maier, W.F.; Hempelmann, R.; Bulan, A.; Kintrup, J.; Weber, R. In situ Supported Nanoscale $Ru_xTi_{1-x}O_2$ on Anatase TiO2 with Improved Electroactivity. *Chem. Mater.* **2010**, *22*, 6215–6217. [CrossRef]

40. Zhu, X.; Wang, P.; Wang, Z.; Liu, Y.; Zheng, Z.; Zhang, Q.; Zhang, X.; Dai, Y.; Whangbo, M.-H.; Huang, B. Co_3O_4 nanobelt arrays assembled with ultrathin nanosheets as highly efficient and stable electrocatalysts for the chlorine evolution reaction. *J. Mater. Chem. A* **2018**, *6*, 12718–12723. [CrossRef]

41. Moreno-Hernandez, I.A.; Brunschwig, B.S.; Lewis, N.S. Crystalline nickel, cobalt, and manganese antimonates as electrocatalysts for the chlorine evolution reaction. *Energy Environ. Sci.* **2019**, *12*, 1241–1248. [CrossRef]

42. Liu, J.; Hinsch, J.J.; Yin, H.; Liu, P.; Zhao, H.; Wang, Y. TMN$_4$ complex embedded graphene as efficient and selective electrocatalysts for chlorine evolution reactions. *J. Electroanal. Chem.* **2022**, *907*, 116071. [CrossRef]

43. Dickens, C.F.; Nørskov, J.K. A Theoretical Investigation into the Role of Surface Defects for Oxygen Evolution on RuO2. *J. Phys. Chem. C* **2017**, *121*, 18516–18524. [CrossRef]

44. Rao, R.R.; Kolb, M.J.; Halck, N.B.; Pedersen, A.F.; Mehta, A.; You, H.; Stoerzinger, K.A.; Feng, Z.; Hansen, H.A.; Zhou, H.; et al. Towards identifying the active sites on RuO_2(110) in catalyzing oxygen evolution. *Energy Environ. Sci.* **2017**, *10*, 2626–2637. [CrossRef]

45. Kresse, G.; Hafner, J. Ab initio molecular dynamics for liquid metals. *Phys. Rev. B* **1993**, *47*, 558. [CrossRef]

46. Kresse, G.; Furthmüller, J. Efficiency of ab-initio total energy calculations for metals and semiconductors using a plane-wave basis set. *Comput. Mater. Sci.* **1996**, *6*, 15–50. [CrossRef]

47. Perdew, J.P.; Burke, K.; Ernzerhof, M. Generalized Gradient Approximation Made Simple. *Phys. Rev. Lett.* **1996**, *77*, 3865–3868. [CrossRef]

48. Kresse, G.; Joubert, D. From ultrasoft pseudopotentials to the projector augmented-wave method. *Phys. Rev.* **1999**, *59*, 1758–1775. [CrossRef]

49. Grimme, S.; Antony, J.; Ehrlich, S.; Krieg, H. A consistent and accurate ab initio parametrization of density functional dispersion correction (DFT-D) for the 94 elements H-Pu. *J. Chem. Phys.* **2010**, *132*, 154104. [CrossRef]

50. Dobson, J.F.; Gould, T. Calculation of dispersion energies. *J. Phys. Condens. Matter.* **2012**, *24*, 073201. [CrossRef]

51. Bjorkman, T.; Gulans, A.; Krasheninnikov, A.V.; Nieminen, R.M. Are we van der Waals ready? *J. Phys. Condens. Matter* **2012**, *24*, 424218. [CrossRef] [PubMed]

52. Dobson, J.F.; White, A.; Rubio, A. Asymptotics of the Dispersion Interaction: Analytic Benchmarks for van der Waals Energy Functionals. *Phys. Rev. Lett.* **2006**, *96*, 073201. [CrossRef] [PubMed]

53. Sun, T.; Wang, Y.; Zhang, H.; Liu, P.; Zhao, H. Adsorption and oxidation of oxalic acid on anatase TiO2 (001) surface: A density functional theory study. *J. Colloid Interface Sci.* **2015**, *454*, 180–186. [CrossRef] [PubMed]

54. Dronskowski, R.; Bloechl, P.E. Crystal orbital Hamilton populations (COHP): Energy-resolved visualization of chemical bonding in solids based on density-functional calculations. *J. Phys. Chem.* **1993**, *97*, 8617–8624. [CrossRef]

55. Deringer, V.L.; Tchougreeff, A.L.; Dronskowski, R. Crystal orbital Hamilton population (COHP) analysis as projected from plane-wave basis sets. *J. Phys. Chem. A* **2011**, *115*, 5461–5466. [CrossRef]

56. Maintz, S.; Deringer, V.L.; Tchougreeff, A.L.; Dronskowski, R. Analytic projection from plane-wave and PAW wavefunctions and application to chemical-bonding analysis in solids. *J. Comput. Chem.* **2013**, *34*, 2557–2567. [CrossRef]

57. Maintz, S.; Deringer, V.L.; Tchougreeff, A.L.; Dronskowski, R. LOBSTER: A tool to extract chemical bonding from plane-wave based DFT. *J. Comput. Chem.* **2016**, *37*, 1030–1035. [CrossRef]

58. Nelson, R.; Ertural, C.; George, J.; Deringer, V.L.; Hautier, G.; Dronskowski, R. LOBSTER: Local orbital projections, atomic charges, and chemical-bonding analysis from projector-augmented-wave-based density-functional theory. *J. Comput. Chem.* **2020**, *41*, 1931–1940. [CrossRef]

59. Nørskov, J.K.; Bligaard, T.; Logadottir, A.; Kitchin, J.R.; Chen, J.G.; Pandelov, S.; Stimming, U. Trends in the Exchange Current for Hydrogen Evolution. *J. Electrochem. Soc.* **2005**, *152*, J23. [CrossRef]